International Journal of Extreme Manufacturing

Nanosecond laser shock detonation of nanodiamonds: from laser-matter interaction to graphite-to-diamond phase transition

OPEN ACCESS
IOP Publishing | IMMT
International Journal of Extreme Manufacturing
Int. J. Extrem. Manuf. 4 (2022) 015401 (12pp)
https://doi.org/10.1088/2631-7990/ac37f1

Nanosecond laser shock detonation of nanodiamonds: from laser-matter interaction to graphite-to-diamond phase transition

Xing Zhang[1], Haofan Sun[2], Bo Mao[3], Rui Dai[2], Houlong Zhuang[2], Yiliang Liao[1,*] and Qiong Nian[2,*]

[1] Department of Industrial and Manufacturing Systems Engineering, Iowa State University, Ames, IA 50011, United States of America
[2] School of Engineering for Matter, Transport and Energy, Arizona State University, Tempe, AZ 85287, United States of America
[3] School of Materials Science and Engineering, Shanghai Jiao Tong University, Shanghai 200240, People's Republic of China

E-mail: leonl@iastate.edu and qiong.nian@asu.edu

Received 26 May 2021, revised 28 July 2021
Accepted for publication 8 November 2021
Published 25 November 2021

Abstract

Nanodiamonds (NDs) have been widely explored for applications in drug delivery, optical bioimaging, sensors, quantum computing, and others. Room-temperature nanomanufacturing of NDs in open air using confined laser shock detonation (CLSD) emerges as a novel manufacturing strategy for ND fabrication. However, the fundamental process mechanism remains unclear. This work investigates the underlying mechanisms responsible for nanomanufacturing of NDs during CLSD with a focus on the laser-matter interaction, the role of the confining effect, and the graphite-to-diamond transition. Specifically, a first-principles model is integrated with a molecular dynamics simulation to describe the laser-induced thermo-hydrodynamic phenomena and the graphite-to-diamond phase transition during CLSD. The simulation results elucidate the confining effect in determining the material's responses to laser irradiation in terms of the temporal and spatial evolutions of temperature, pressure, electron number density, and particle velocity. The integrated model demonstrates the capability of predicting the laser energy threshold for ND synthesis and the efficiency of ND nucleation under varying processing parameters. This research will provide significant insights into CLSD and advance this nanomanufacturing strategy for the fabrication of NDs and other high-temperature-high-pressure synthesized nanomaterials towards extensive applications.

Keywords: nanodiamond, confined laser shock detonation, first-principles modeling, molecular dynamics simulation, graphite-to-diamond transition

* Authors to whom any correspondence should be addressed.

2631-7990/22/015401+12$33.00

1. Introduction

Nanosized diamond particles, namely nanodiamonds (NDs), have drawn enormous attention in recent years due to their remarkable mechanical and optical properties, high biocompatibility, rich surface chemistry, wide bandgap, and high field emission [1–4]. NDs have been extensively studied for widespread applications in drug delivery [5], optical bioimaging [6], sensors [7], quantum computing [8], etc. However, manufacturing NDs is difficult, costly, and energy intensive. To synthesize NDs, existing methods often promote the graphite-to-diamond phase transition through a high-temperature-high-pressure (HTHP) chemical detonation process [9, 10], which suffers from poor controllability and significant safety issues. Furthermore, chemical explosives and dynamic shock compression induced by high-energy pulsed lasers have been employed recently for nanomanufacturing of NDs [11, 12]. Specifically, an intense ultrashort pulsed laser beam is applied to trigger the instantaneous vaporization and ionization of graphite, leading to the formation of plasma with a peak pressure of tens of GPa and a maximum temperature of thousands of K [13, 14]. The subsequent expansion of laser-induced plasma drives a shockwave into the material favoring the graphite-to-diamond phase transition. In the work of Kraus *et al* [12], two nanosecond high-energy pulsed laser beams were focused onto a pyrolytic graphite bulk, leading to a maximum shockwave pressure of 228 GPa for ND fabrication. The *in-situ* x-ray diffraction characterization indicated that the graphite-to-diamond transition occurred at 20 GPa and the transition rate increased with the increase of peak pressure/laser energy. However, the applied pulsed laser energy ($\geqslant$32 kJ cm^{-2} per pulse) is dramatically higher than that in other laser-based processes [15–17] (tens of J cm^{-2} per pulse), which induces the air breakdown phenomenon [18]. Therefore, a tightly controlled vacuum system and intensive laser power energy are required, leading to a complex experimental apparatus and tedious procedures.

To realize scalable nanomanufacturing of NDs in the ambient environment, a simple, cost-effective approach, called confined laser shock detonation (CLSD), was developed in recent years [19]. It is hypothesized that by taking advantages of the confining effect, which restricts the hydrodynamic expansion of laser-induced plasma in laser shock processing [20, 21], a moderate-energy laser pulse can be applied to introduce the localized HTHP condition that triggers the graphite-to-diamond transition under room-temperature, non-vacuum processing. The experimental investigations in our previous work [19] demonstrated the feasibility of CLSD for nanomanufacturing of NDs. Given the confining effect introduced by two pieces of tightly clamped transparent BK-7 glasses, NDs with a diameter of tens of nanometers were successfully manufactured using CLSD with a laser influence as low as $\sim$100 J cm^{-2} per pulse. The experimental investigations demonstrated that the growth of NDs during CLSD is dominated by the plasma dynamics attributed to the laser-matter interaction. However, due to the complexity and limitations of *in-situ* characterization of laser shock processing, a comprehensive investigation on the plasma physics responsible for the graphite-to-diamond transition remains a challenge. Particular scientific questions to be answered include: (a) how the confining effect alters the laser-matter interaction in terms of temperature and pressure evolutions; (b) how the spatial and temporal variations of plasma/shockwave characteristics affect the nucleation and growth of NDs; and (c) how the graphite-to-diamond transition rate is affected by CLSD processing conditions.

In order to elucidate the underlying mechanisms responsible for ND formation, in this work, a physics-based modeling framework is developed by integrating a first-principles model describing the laser-matter interaction with a molecular dynamics (MD) simulation predicting the graphite-to-diamond transition. The material responses to laser irradiation including the temporal and spatial evolutions of temperature, pressure, electron number density and particle velocity are investigated. The confining effect on the laser-matter interaction, plasma characteristics, and shockwave generation/propagation is elucidated. The crystallography changes of carbon structure as affected by thermal and pressure loadings are analyzed. The graphite-to-diamond transition rate subjected to CLSD processing parameters is studied. We envision that the knowledge gained in this work will advance the design and optimization of CLSD for scalable nanomanufacturing of NDs towards extensive applications.

2. Experimental design

CLSD experiments were performed using the setup shown in figure 1(a). A 50 μm-thick graphite layer was spray coated onto a BK7 glass (McMaster-Carr), using a commercially available graphite lubricant (Asbury Carbons Inc.). After drying, another BK7 glass was placed on top of the graphite layer where it acted as a rigid transparent confinement to maximize the confining effect. A Surelite III Nd-YAG laser (Continuum Inc.) with a wavelength of 1064 nm and a pulse duration of 7 ns was used as the laser source. The laser beam size at the graphite surface was controlled by an F-theta lens. After laser processing, the material within processed area was collected and dispersed into toluene for further analysis. The microstructural characterization was carried out by a Titan 80–300 kV environmental electron microscope. Figure 1(b) presents the bright field high-resolution transmission electron microscopy image of the sample processed with a laser fluence of 200 J cm^{-2}, which reveals a few laser-fabricated nanocrystals (<10 nm in diameter, marked by white arrows) that possess lattice structures that differ from the surrounding graphite. The higher-magnification image and lattice profile inset, as shown in figure 1(c), demonstrate an inter-planar spacing of 0.253 nm of the nanocrystals, which matches the (220) *d*-spacing of the diamond structure [22, 23]. Figure 1(c) inset also shows the corresponding fast Fourier transform patterns, indicating a high crystal quality of CLSD-fabricated NDs. These experimental investigations confirm the feasibility of our CLSD setup for achieving the graphite-to-diamond transition with a low laser energy (200 J cm^{-2}), as compared to that ($\geqslant$32 kJ cm^{-2}) used in Kraus's work [12].

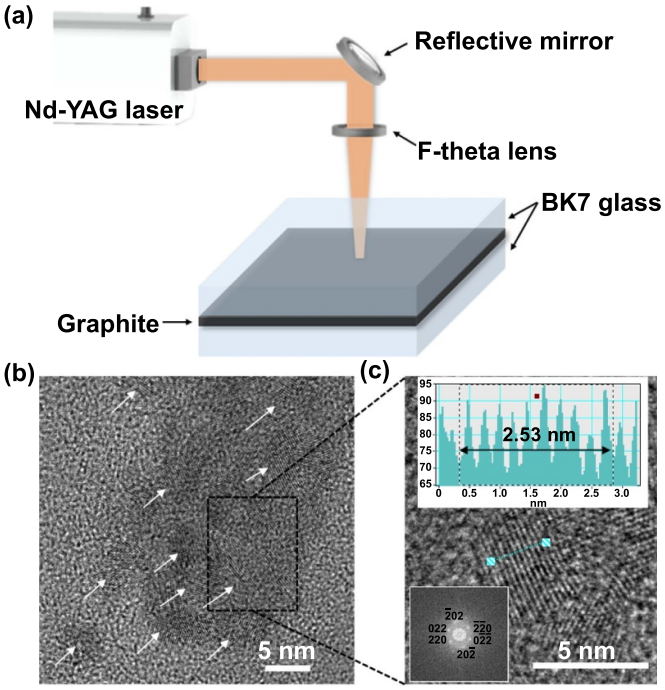

Figure 1. (a) Schematic illustration of CLSD experimental setup. (b) Bright field HRTEM image of CLSD-processed area, with NDs marked by white arrows. (c) Enlarged HRETEM image of selected NDs, with lattice profile and FFT pattern inserted.

3. Computational modeling

A theoretical model integrating a first-principles model with MD simulations was developed to elucidate the process mechanism. We employed the first-principles model to describe the laser-matter interaction and the thermo-hydrodynamic phenomena during the CLSD process. The outputs of the first-principles model in terms of the thermal and shock loadings were used as input variables for MD simulations. The MD simulations were carried out to simulate the carbon bond reconfiguration and correlate the graphite-to-diamond transition rate with laser processing parameters.

3.1. First-principles modeling of laser-matter interaction

In the CLSD process, the absorbed laser energy is first redistributed among the free electrons by electron-electron collisions and then thermalized into electron gas within the femtosecond regime, and, later on, transferred to the ions via electron-phonon collisions within picosecond regime [24, 25]. Given a high laser energy input, only a small portion of energy is used to heat the target material above the critical temperature to form plasma. The rest of laser energy is absorbed by plasma via the inverse Bremsstrahlung or photoionization process, depending on the target material and the laser wavelength [26]. To describe the laser-matter interaction, a series of conservation laws was employed for predicting the thermodynamic and/or hydrodynamic characteristics of the laser-irradiated material, including temperature, pressure, electron number density, and particle velocity. The first-principles modeling framework capable of describing the laser energy absorption, plasma formation and expansion during pulsed laser shock processing was developed in our previous work [27].

The formation of laser-induced plasma due to laser energy absorption was considered using the energy conservation equations, also known as the two-temperature model which describes the thermal diffusion of electrons and ions as [27]:

$$\begin{cases} C_{\mathrm{e}}\dfrac{\partial T_{\mathrm{e}}}{\partial t} = \nabla\cdot(k_{\mathrm{e}}\nabla T_e) - \Gamma_{\mathrm{ei}}(T_{\mathrm{e}}-T_{\mathrm{i}}) - \left(\dfrac{\partial E_{\mathrm{e}}}{\partial V}+p_{\mathrm{e}}\right)\dfrac{\partial V}{\partial t} \\ \qquad\qquad +R_{\mathrm{Abs}} - R_{\mathrm{Emis}} + S \\ C_{\mathrm{i}}\dfrac{\partial T_{\mathrm{i}}}{\partial t} = \nabla\cdot(k_i\nabla T_{\mathrm{i}}) + \Gamma_{\mathrm{ei}}(T_{\mathrm{e}}-T_{\mathrm{i}}) - \left(\dfrac{\partial E_{\mathrm{i}}}{\partial V}+p_{\mathrm{i}}\right)\dfrac{\partial V}{\partial t} \\ \qquad\qquad -q\dfrac{\partial V}{\partial t} \end{cases}, \tag{1}$$

where C_{e} and C_{i} are the specific heat capacities, T_{e} and T_{i} are the temperatures, k_{e} and k_{i} are the thermal conductivities, E_{e} and E_{i} are the specific internal energies, and p_{e} and p_{i} are the energy densities. The subscripts 'e' and 'i' represent the parameters for electrons and ions, respectively. In addition, t is the time, V is the specific volume, and Γ_{ei} is the electron-phonon coupling constant that describes the energy exchange rate between electrons and ions. The radiation absorption R_{Abs} and emission R_{Emis} caused by the high-temperature plasma are considered as [28]:

$$R_{\mathrm{Abs}} = c\sum\nolimits_{\mathrm{g}}^{N_{\mathrm{F}}}(\sigma_{\mathrm{g}}^{\mathrm{PA}}E_{\mathrm{R,g}}), \tag{2}$$

$$R_{\mathrm{Emis}} = \frac{8\pi(k_{\mathrm{B}}T_{\mathrm{e}})^4}{c^2h^3}\sum\nolimits_{\mathrm{g}}^{N_{\mathrm{F}}}\left(\sigma_{\mathrm{g}}^{\mathrm{PE}}\int_{x_{\mathrm{g}}}^{x_{\mathrm{g}+1}}\mathrm{d}x\frac{x^3}{e^x-1}\right), x=\frac{hw}{kT_{\mathrm{e}}}, \tag{3}$$

where g is the frequency group index, N_{F} is the number of frequency groups, h is Planck's constant, c is the speed of light, w is the angular frequency, $E_{\mathrm{R,g}}$ is the radiation energy density of the groups, and ${\sigma_{\mathrm{g}}}^{\mathrm{PA}}$ and ${\sigma_{\mathrm{g}}}^{\mathrm{PE}}$ are Planck mean opacities for absorption and emission, respectively. The incident laser pulse can be given by [29]:

$$S = \alpha(1-R)I(t)\mathrm{e}^{-2{r_{\mathrm{c}}}^2/{r_0}^2}\mathrm{e}^{-\alpha z}, \tag{4}$$

where R is the reflectvitiy of material to laser, $I(t)$ is the laser intensity as a function of time, r_0 is the radius of the laser beam, r_{c} is the radial coordinate, z is the depth measured from the target surface, and α is the absoprtion coefficient. The term $\alpha\mathrm{e}^{-\alpha z}$ represents the energy attenuation as the laser beam travels inwards into the material. In this model, when a high-energy beam is irradiated onto the target surface and instantaneously form a layer of plasma, the laser energy absorbed by the plasma plume is determined by an inverse Bremsstrahlung model, where the absorption coefficient can be written as [30]:

$$\alpha = (2\pi)^{1/2}\left(\frac{16\pi}{3}\right)\frac{\mathrm{e}^6}{c(m_{\mathrm{e}}k_{\mathrm{B}}T_{\mathrm{e}})^{3/2}}Zn_{\mathrm{e}}^2\frac{\ln\Lambda}{w_{\mathrm{L}}^2\sqrt{1-(w_{\mathrm{p}}/w_{\mathrm{L}})^2}}, \tag{5}$$

where n_e is the electron number density, e is the electron charge, m_e is the electron mass, Z is the mean plasma charge, w_p is the plasma frequency, and w_L is the laser frequency. Accordingly, the absorption coefficient α increases with the increase of electron number density n_e. However, as the n_e increases to a critical value n_{ec}, where the local plasma frequency is equal to the laser frequency ($w_p = w_L$), reflection occurs. As a result, laser energy that passes beyond a critical surface is ignored in this model, and the critical number density can be calculated by [31]:

$$n_{ec} = 1.1 \times 10^{21} (\lambda^{-2}) \, \mathrm{cm}^{-3}, \tag{6}$$

where λ is the wavelength of laser beam in μm.

Furthermore, the hydrodynamic expansion of laser-induced plasma can be analyzed in Lagrangian coordinates, where the spatial grids move with the plasma plume without varying the mass of each volume element. Therefore, the mass conservation equation can be given as [28, 30]:

$$\frac{\partial V}{\partial t} = \frac{\partial u}{\partial m_0}, \tag{7}$$

where u is the particle velocity and m_0 is the Lagrangian mass variable. The mass density is calculated at each time step using the updated velocities. The momentum conservation equation can be solved using one-fluid approximation, which assumes electrons and ions flow together [28, 30]:

$$\frac{\partial u}{\partial t} = -\frac{\partial}{\partial m_0}(P + q) + \Delta u, \tag{8}$$

where P is the total pressure contributed from ions, electrons, and radiations, q is the von Neumann artificial viscosity, and Δu is the velocity change due to momentum exchange from decelerating fast particles. By solving the major equations (1), (7) and (8), the material responses as functions of time and space during and after the irradiation of an ultrashort laser pulse can be obtained. The detailed formulations of various coefficients/material properties and the applied finite difference method can be found in prior reports [27, 30].

In this work, a 1-D radiation-magnetohydrodynamics code (HELIOS-CR) developed by MacFarlane *et al* was used as a computational platform to perform the first-principles modeling. The material properties in the current study were based on PROPACEOS tables [30]. We focused on the study of CLSD using a nanosecond pulsed laser that has a Gaussian beam profile, with a wavelength of 1064 nm, a pulse duration of 5–25 ns, and a laser fluence of 100–1400 J cm^{-2}. Since the applied pulse duration is much longer than the ion heating time via electron-phonon collisions, it is reasonable to assume that the local thermal equilibrium ($T_i = T_e$) can be instantaneously reached during CLSD. In addition, the laser beam size is typically much larger than the thermal penetration depth, thus, the model can be re-established with one-dimensional approximation. Figure 2 illustrates the modeling configurations used in this work, including cases of LSD without confinement and CLSD for comparison purposes. A 100 μm-thick graphite layer was placed on top of a 3 mm-thick SiO_2 glass.

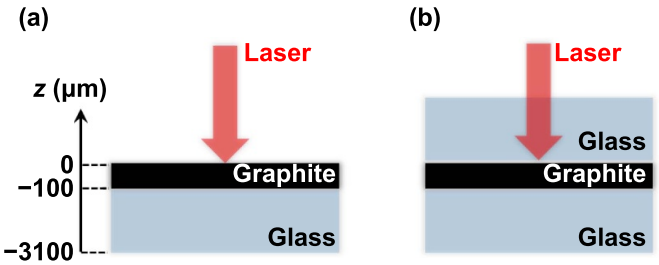

Figure 2. Configurations of first-principles model: (a) LSD without confinement, and (b) CLSD.

The pulsed laser was irradiated onto the graphite top surface at $z = 0$ μm (figure 2(a)). For the simulation case of CLSD, the second 3 mm-thick glass was placed on top of the graphite to investigate the effect of a rigid confinement on the plasma plume, which resembles our CLSD experimental setup.

3.2. MD simulation of carbon phase transition

With the thermal and shock loading inputs from the first-principles modeling, MD simulations were performed to simulate the carbon bond reconfiguration for the graphite-to-diamond phase transition. The Large-scale Atomic/Molecular Massively Parallel Simulator (LAMMPS) package was employed for MD simulation [32]. Firstly, the graphite structure was created in x, y, and z-directions with 1200 atoms in six layers and confined in a rigid simulation box with a size of 25.0 × 22.0 × 20.0 nm^3. Periodic boundary conditions were applied in all three directions to approximate the behavior of macro-scale systems and minimize the edge effect. The resulting graphite structure was subjected to the system's temperature and pressure, corresponding to the thermal and shock loadings obtained from the first-principles model. Finally, the reconfiguration of carbon bonds and restructuring of the graphite crystallography structure under various laser processing conditions were extracted and analyzed. To describe the movement of carbon atoms, we applied a previously developed adaptive intermolecular reactive empirical bond order potential (AIREBO), composed of covalent bonding REBO interaction, Lenard-Jones (L-J) intermolecular potential, and torsion interaction. By using the AIREBO potential, the conjugation effect between the different atoms was accurately handled by correcting the bond order term, which accounts for the sp^3 carbon bonds; introducing L-J interaction can correctly describe the compressed graphite structure [33]. To obtain reliable and repeatable results, all samples were relaxed at 300 K and were traction free for 4.2 ns MD time based on a non-equilibrium MD simulation [34]. Three different system temperatures of 2500, 3500, and 4500 K (approximately 0.21, 0.30, and 0.39 in the unit of eV) were applied by manually adding kinetic energy into carbon atoms to study the effect of activation energy on the carbon phase transition in the CLSD process. No higher system temperature was applied to keep the material in solid state according to the carbon phase diagram. Five different system pressures of 11, 22, 33, 44, and 55 GPa (selected on basis of first

principal model outputs corresponding to varying laser energy inputs), were manually controlled to investigate the carbon atoms' relocation and carbon bonds' reconfiguration. All of the MD snapshots and videos were visualized using OVITO [35]. A pair distribution function $g(r)$, which describes the probability of identifying two carbon atoms separated by a specific distance r, was applied to evaluate the atomic structure change during phase transition [36].

4. Results and discussion

4.1. Thermo-hydrodynamics during LSD without confinement

To understand the confining effect during CLSD, LSD without confinement (figure 2(a)) was first studied, with a focus on the laser-induced thermo-hydrodynamic phenomena. Given a laser fluence of 400 J cm^{-2}, a pulse duration of 10 ns, and a delay time of 5 ns, the contour plot of the first-principles-simulated temporal and spatial evolution of temperature is shown in figure 3(a). When the pulsed laser energy irradiated the target, the surface material experienced an instantaneous increase in temperature (up to tens of eV), leading to material ablation and plasma formation. The temperature (T) rises to a maximum value of 49.8 eV at $t = 6.7$ ns, shortly after the laser energy reaches its peak value at 5 ns. It was observed that due to lack of confining effect, the high-temperature region (>45 eV) was located within the free space ($z > 0$ μm) rather than at the graphite surface ($z = 0$ μm), where the initial laser-matter interaction occurs and, later, expanded away from the solid graphite. On the other hand, an insignificant temperature rise was found at the graphite layer ($z \leqslant 0$ μm) during LSD. Figure 3(b) demonstrates the detailed temporal evolutions of temperature at different locations near the initial graphite surface. At $z = 250$ μm (in the free space), the temperature rapidly increased to a maximum value of 45 eV and cooled down at a slower rate. The tail shows that the temperature at this location stayed around 5 eV for over 200 ns, which is much longer than the laser pulse duration of 10 ns. Additionally, it was found that the maximum temperature reduced when moving toward the graphite layer. At $z = 50$ μm, the temperature reached its peak value of 5.5 eV at $t = 20$ ns. At the top surface of the graphite ($z = 0$ μm), the temperature slowly increased to 3 eV at $t = 200$ ns. At $z = -2$ μm (underneath the graphite top surface), the temperature increased but did not exceed 1 eV. The shift of temperature peaks is caused by the heat transfer from the higher temperature region to the lower ones.

Figure 3(c) captures the electron number density (n_e) evolution near the graphite's top surface, where a recessed interface (marked by white dashed line) between non-vaporized and vaporized/ionized graphite can be identified. Such recession is caused by laser ablation and compression of graphite layers. Above this interface, n_e gradually decreased with increasing z due to the plasma plume expanding into the free space. The detailed spatial distributions of n_e at different time steps are depicted in figure 3(d). The right inset figure magnifies the n_e evolution above the initial graphite surface at 0 μm $< z <$ 50 μm, where the critical surface with an electron density of 1.1×10^{21} cm^{-3} (n_{ec} calculated according to equation (6)) can be located in the plasma plume. This critical surface shielded the material from later beam irradiation after plasma formation. Thus, the transportation of later absorbed energy to regions underneath the critical surface (including dense regions of plasma plume within which $n_e > n_{ec}$ and the non-vaporized graphite) is mostly achieved by thermal conduction. Furthermore, it appears that the critical surface swiftly advanced towards the free space as the laser-matter interaction proceeded due to the continuously free expansion of the plasma plume, resulting in the highest-temperature regions rapidly escaping away from the initial graphite surface. Consequently, only a limited amount of heat transferred to the graphite via thermal conduction, and the temperature rose to only a few eV within a thin graphite layer, as shown in figures 3(a) and (b). The left inset figure in figure 3(d) details the n_e evolution underneath the initial graphite surface at -70 μm $< z < 0$ μm. It is found that n_e of some non-vaporized graphite layers slightly increased, which could be attributed to the compression of volume elements. Such a compression effect represents the shockwave being driven into the graphite as a consequence of plasma expansion, and the shockwave front can be determined at the locations where n_e ceases to increase, i.e. -36 μm at $t = 6$ ns and -50 μm at $t = 9$ ns. From figures 3(c) and (d), the shockwave propagating inside the material can be clearly observed and its front velocity can be calculated accordingly.

Moreover, the evolutions of pressure and particle velocity can be predicted via the first-principles model. Figure 4(a) plots the temporal and spatial evolution of pressure with a maximum value of 4.5 GPa at $t = 6.7$ ns, given LSD processing parameters of 400 J cm^{-2} laser fluence, 10 ns pulse duration, and 5 ns delay time. Due to the ejection of ionized particles into the free space and the resulting reaction force on the graphite layers, two pressure peaks travelling in opposite directions can be observed at both sides of the initial graphite surface. The one travelling in the free space indicates plasma expansion and the other one travelling in the non-vaporized graphite indicates shockwave propagation. Figure 4(b) shows the spatial distribution of pressure at different time steps. It can be observed that the plasma peak pressure was lower than the shockwave peak pressure. Overtime, the shockwave peak pressure shows a smaller reduction of magnitude and a slower propagation rate due to the presence of the solid material. By comparing figure 4(a) with figure 3(a), it can be concluded that the high-pressure shockwave had a much higher penetration depth and larger traveling velocity in the graphite than the heat conduction. For example, at $t = 20$ ns, the graphite layer at $z = -50$ μm reached a maximum pressure of 2.9 GPa and still remained at room temperature. Figure 4(c) shows the temporal and spatial evolution of particle velocity during LSD without confinement, which has a similar shape to the plasma pressure distribution. The particles ejected into the free space reached the highest velocity at the same location in the plasma pressure peak, with the lowest velocity (close to $z = 0$ μm) at the graphite surface. In addition, the particle velocity peak advances towards the free space and its value gradually decreases as time passes due to the free expansion, as shown in figure 4(d).

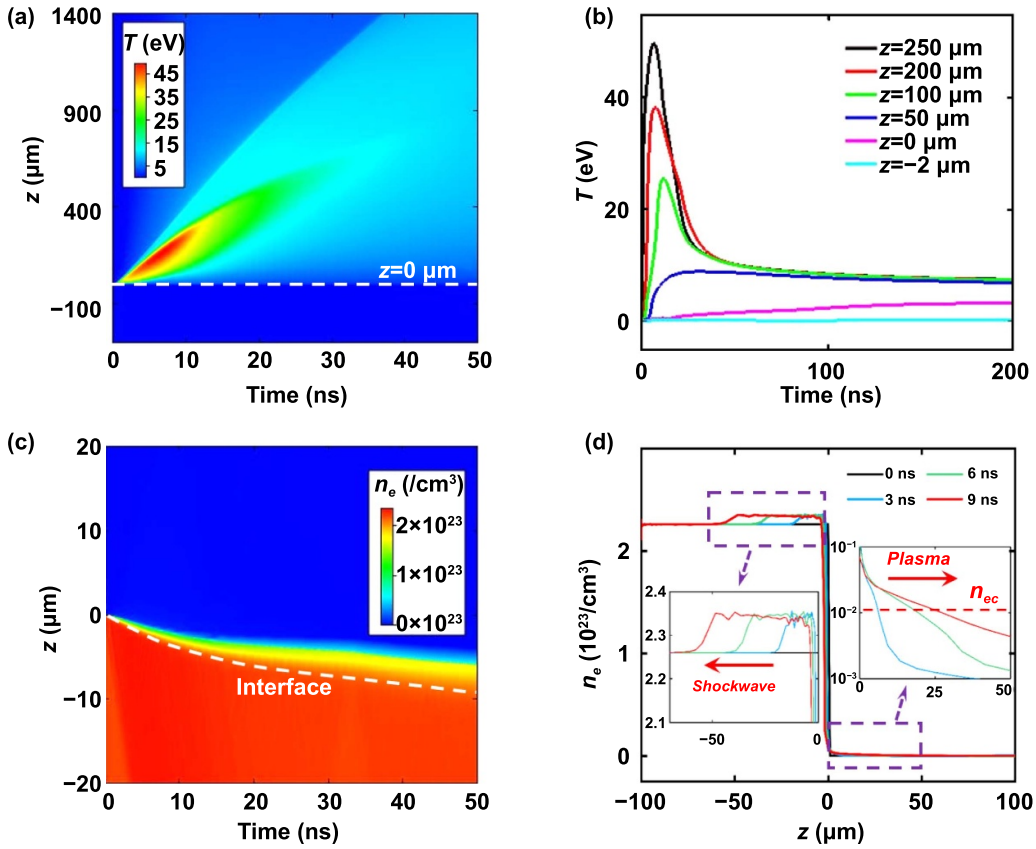

Figure 3. Simulated evolutions of temperature (T) and electron number density (n_e) during LSD without confinement (400 J cm^{-2} laser fluence, 10 ns pulse duration, and 5 ns delay time): (a) temporal and spatial evolution of temperature; (b) temporal evolution of temperature at different locations; (c) temporal and spatial evolution of electron number density; and (d) spatial evolution of electron number density at different time steps.

4.2. Thermo-hydrodynamics during CLSD

To investigate the thermo-hydrodynamic phenomena as affected by the confining effect, CLSD with a rigid confinement (figure 2(b)) was simulated and compared to the results in section 4.1. Given the laser processing parameters of 400 J cm^{-2} laser fluence, 10 ns pulse duration, and 5 ns delay time, the material responses as functions of time and space are plotted in figure 5, showing near-symmetrical shapes. Figure 5(a) indicates the temperature evolution with a maximum value of 26 eV at $t = 6.7$ ns. The high temperature region (>25 eV) is located near the initial graphite surface. Additionally, the temperature can reach 10 eV at $z = -40$ μm when $t = 50$ ns, indicating a much higher thermal penetration depth as compared to LSD without confinement. Figure 5(b) shows the electron number density distribution, where the recessed interface reaches a depth of $z = -60$ μm at $t = 50$ ns, demonstrating a high level of ablation and compression effects. The presence of the rigid boundary significantly restricted the expansion of the plasma plume, leading to an increase in the electron number density and a decrease in the laser absorption region ($n_e < n_{ec}$), as compared to LSD without confinement. As a result, a relatively lower temperature was observed due to the enhanced laser energy reflection. Furthermore, the shockwave pressure was significantly enhanced, with a maximum value that increased by 455% from 4.5 to 25 GP, as shown in figure 5(c), due to the restricted expansion of each volume element. Moreover, the particle velocity can further indicate the confining effect on enhanced shockwave pressure, as shown in figure 5(d). When the ejected ionized particles hit the top rigid boundary, the particles bounced back towards the graphite layer with the same magnitude of velocity, leading to localized high particle velocity and density conditions which significantly improved shockwave pressure as compared to LSD without confinement.

The above results indicate that the HTHP condition during CLSD with a laser fluence of 400 J cm^{-2} meets the requirements for the graphite-to-diamond phase transition, i.e. temperature above 2000 K (0.17 eV) and pressure above 10 GPa [19]. However, temperature and pressure vary rapidly across spatial locations and time frames, significantly affecting ND formation. To further analyze the potential site and time window for the ND nucleation and growth, detailed temperature and pressure histories at different graphite layers are presented in figures 5(e) and (f). At the initial graphite surface where $z = 0$ μm (figure 5(e)), the temperature and pressure as functions of time show a similar trend. Upon heating, the temperature reaches a few eV, indicating that the

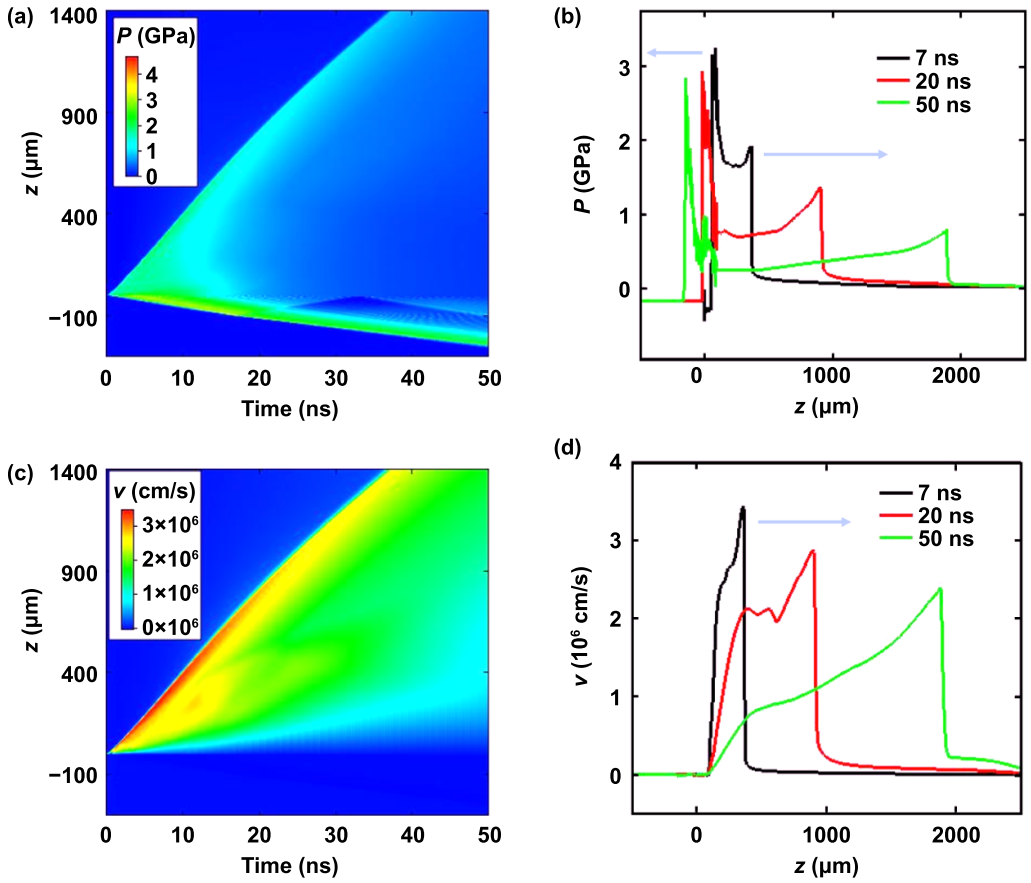

Figure 4. Simulated evolutions of pressure and particle velocity during LSD without confinement (400 J cm^{-2} laser fluence, 10 ns pulse duration, and 5 ns delay time): (a) temporal and spatial evolution of pressure; (b) spatial evolution of pressure at different time steps; (c) temporal and spatial evolution of particle velocity; and (d) spatial evolution of particle velocity at different time steps.

graphite is vaporized/ionized, and thus it is impossible to form long range ordered diamond structure at this stage. During the cooling stage, the pressure decreases synchronously with the temperature. At $t = 60$ ns, when the pressure decreased to 5 GPa, far below the critical value for ND formation, the temperature was still above the melting point of graphite (0.43 eV). Therefore, the graphite-to-diamond phase transition was difficult to initiate at the initial graphite surface. On the other hand, at the newly exposed graphite surface (figure 5(f)), below which the graphite layers stayed in solid-state during CLSD, the temperature rose above 0.17 eV at 9 ns and remained at ∼0.41 eV for over 100 ns. The pressure rapidly increased to 24 GPa at 7 ns and decreased to 10 GPa at 23 ns. Clearly, such HPHT condition within the time domain 9–23 ns (marked by the red area) might be favorable to ND formation. Consequently, the graphite-to-diamond phase transition was expected to occur at the region underneath the initial surface where the target material remained solid state due to a relatively low temperature while the propagated shockwave pressure exceeded the critical value. Additionally, the nucleation and growth of NDs during CLSD may only last for a few ns, which is beneficial to control the ND size distribution. The nucleation of NDs will be investigated via MD simulations in section 4.4.

4.3. Shockwave pressure as affected by processing parameters

The temporal and spatial evolutions of temperature and pressure play two key roles in determining the effectiveness and efficiency of ND fabrication using CLSD. Assuming that the graphite-to-diamond transition mainly takes place near the newly exposed graphite surface where the temperature remains slightly lower than the melting point of graphite (0.43 eV), the laser fluence and pulse duration significantly affect the shockwave peak pressure during laser processing. The simulation results in figure 6 indicate that the peak pressure generally increased with the increase of laser fluence or the decrease of pulse duration for both LSD and CLSD. However, CLSD with a rigid confinement shows a significant enhancement of peak pressure, as compared to LSD without confinement. Such enhancement induced by the confining effect is more significant with the increase of laser fluence or the decrease of pulse duration. For instance, given a laser fluence of 600 J cm^{-2}, the peak pressure increased by 556% from 5.67 to 37.2 GPa after applying the rigid confinement, while a higher laser fluence of 1000 J cm^{-2} achieved a greater enhancement of the peak pressure (635%) from 6.64 to 48.84 GPa. This trend indicates that CLSD is

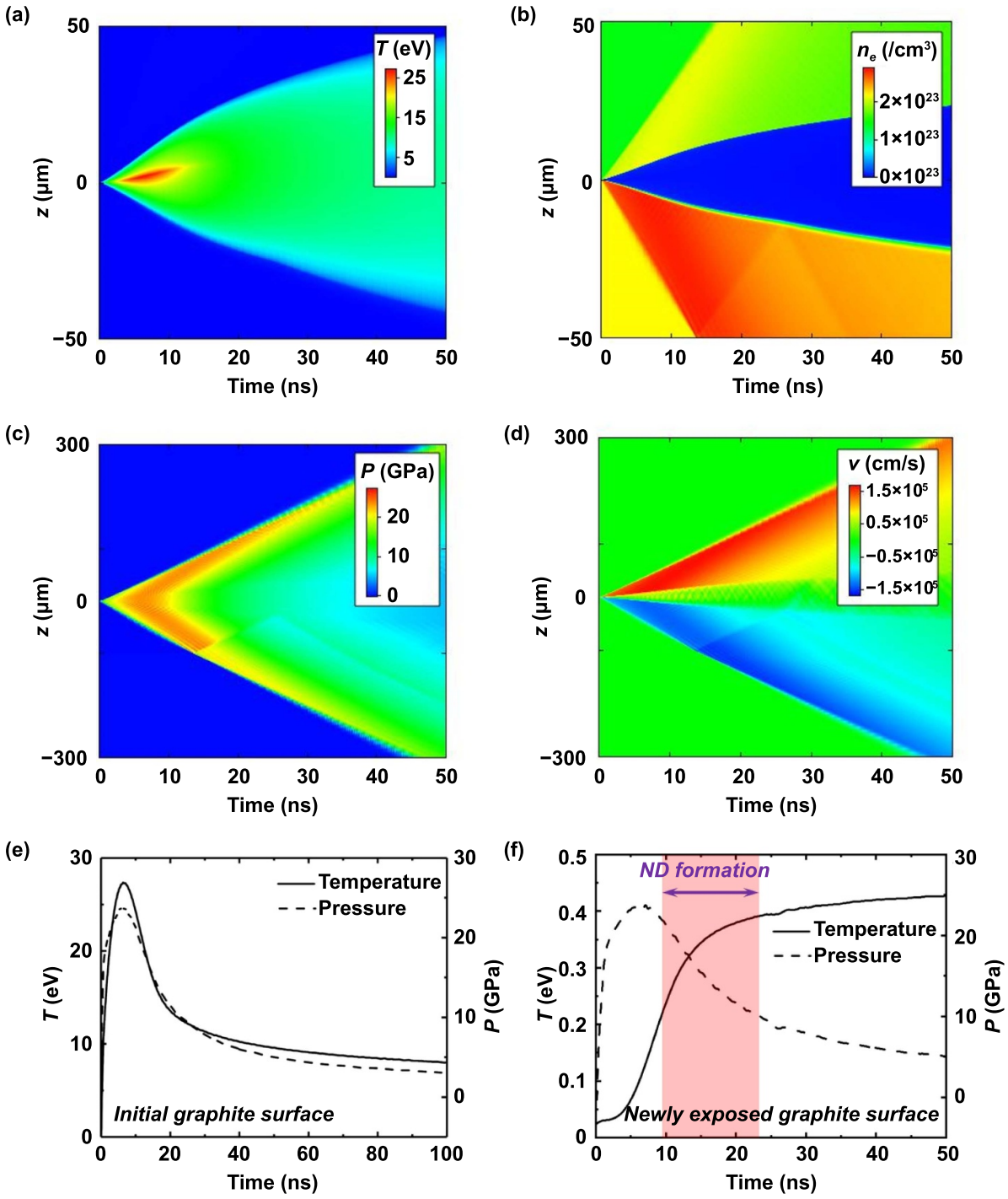

Figure 5. Thermo-hydrodynamic simulations of CLSD with a rigid confinement (400 J cm^{-2} laser fluence, 10 ns pulse duration, and 5 ns delay time): temporal and spatial evolutions of (a) temperature, (b) electron number density, (c) pressure, and (d) particle velocity. The temperature and pressure evolutions at (e) the initial graphite surface ($z = 0$ μm) and (f) the newly exposed graphite surface.

highly efficient in fabricating NDs when increasing the laser energy. More importantly, the utilization of moderate laser energies to induce high pressure makes CLSD more practical for obtaining NDs under ambient conditions. It is also possible to generate extremely high pressure using picosecond or femtosecond pulsed laser and promote the graphite-to-diamond transition [37, 38], which we will explore in a future study.

4.4. MD simulation of ND nucleation

MD simulation were carried out to investigate ND formation under varying HTHP conditions during CLSD. A graphite structure confined in a rigid simulation box was subjected to the system temperature and pressure as two independent laser-induced plasma variables, and the resulting reconfiguration of carbon bonds was extracted and analyzed. Figures 7(a)–(d) show the front and perspective views of the graphite structure

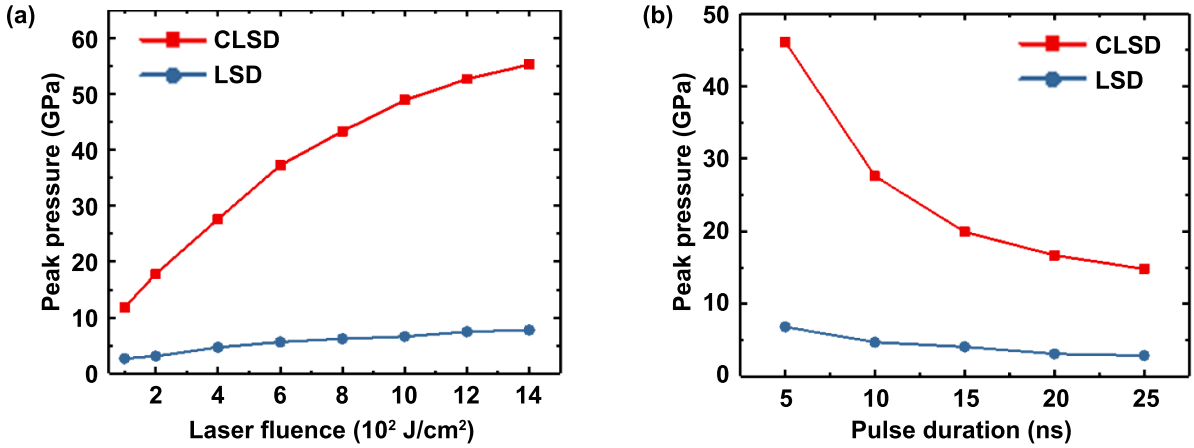

Figure 6. The effects of (a) laser fluence (200–1400 J cm^{-2}) and (b) pulse duration (5–25 ns) on peak pressure during LSD and CLSD.

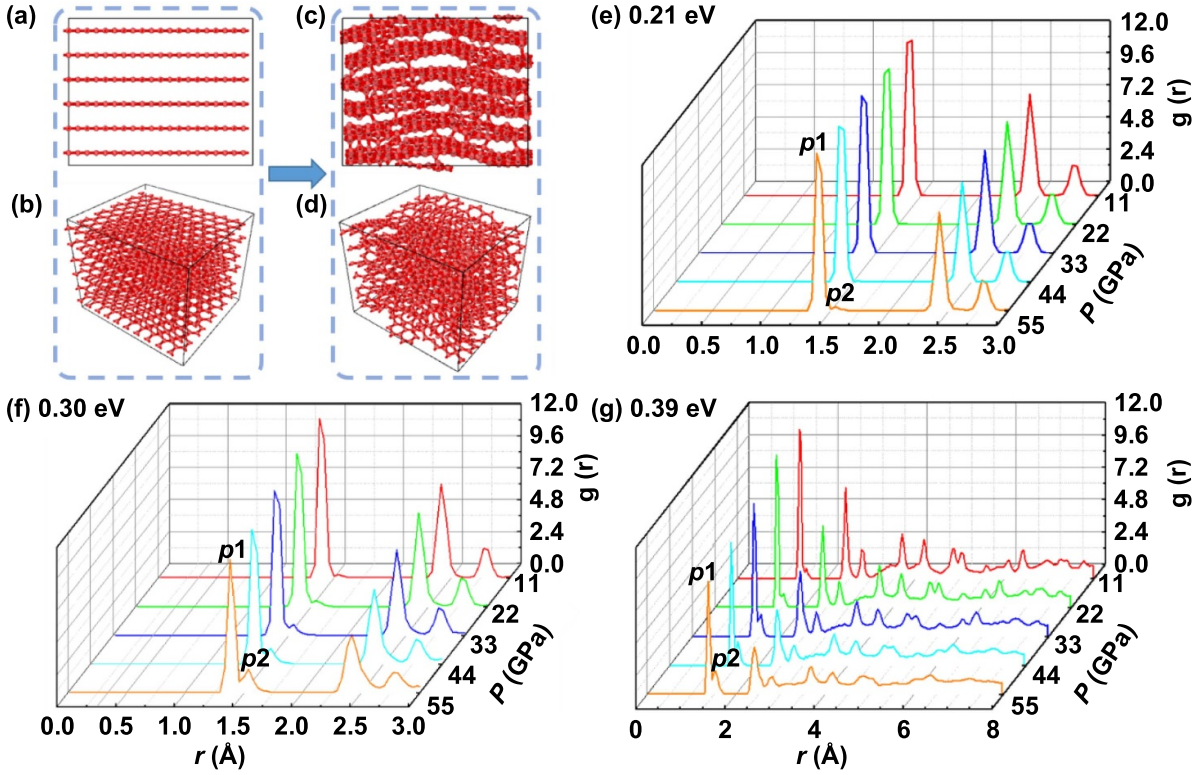

Figure 7. (a) The front view and (b) the perspective view of initial graphite layered structure. (c) The front view and (d) the perspective view of graphite structure after applying an HTHP condition (0.39 eV, 44 GPa), indicating the formation of a diamond-like structure. The $g(r)$-r plots demonstrate the effect of plasma pressure (11–55 GPa) on the carbon bonds' reconfiguration at different temperatures: (e) 0.21 eV, (f) 0.30 eV, (g) 0.39 eV.

before and after applying an HTHP condition (0.39 eV and 44 GPa). A number of vertical carbon bonds formed across the graphite layers, and the positions of the carbon atoms relocated. The movement of the carbon atoms activated by the input kinetic energy formed the sp^3 bond and diamond-like structure. The bond reconfiguration from sp^2 to sp^3 was further confirmed by analyzing the interatomic distance, as demonstrated by the $g(r)$-r plot in figures 7(e)–(g). The marked $p1$ peak at $r = 1.34$ Å stands for the probability of the remaining sp^2–sp^2 carbon bonds, and the $p2$ peak at $r = 1.50$–1.54 Å represents the probability of sp^2–sp^3 and sp^3–sp^3 bonds formed during CLSD. The ratio of $p2/p1$ can be used to evaluate the phase transition rate.

Both temperature and pressure have significantly impact ND formation. Typically, a higher temperature or pressure leads to a higher $p2$ peak, indicating more sp^3 carbon bonds are formed. However, given a temperature of 0.21 eV (figure 7(e)), the height of $p2$ peak is low even with a high system pressure of 55 GPa, showing a relatively low phase transition rate. On the contrary, when the system temperature increased to 0.30 eV (figure 7(f)) and 0.39 eV (figure 7(g)), the $p2$ peaks are clearly observable at a lower system pressure. This can be explained

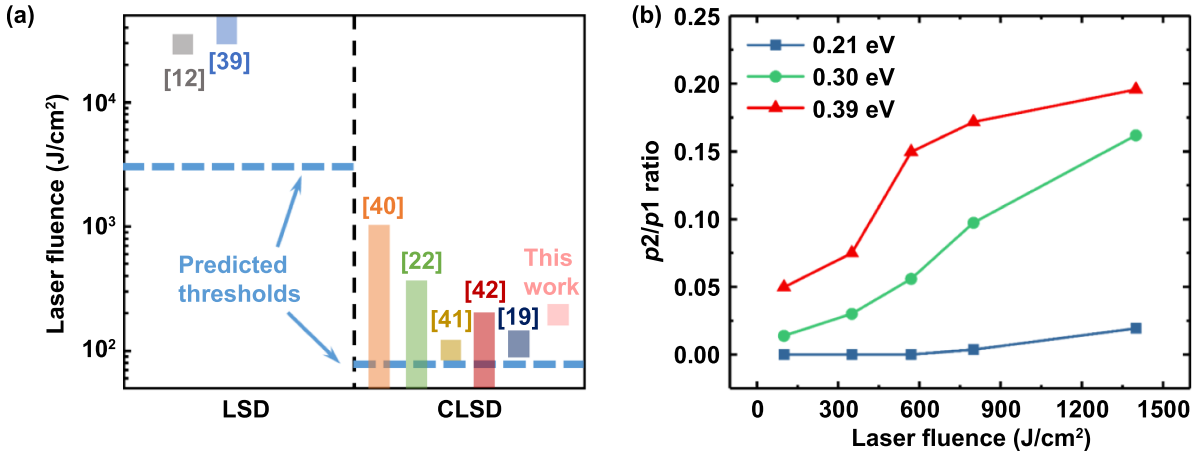

Figure 8. (a) Predicted values of laser fluence threshold (marked by blue dashed lines) and experimental ranges of applied laser fluences (marked by colored columns) for synthesizing NDs during LSD and CLSD. (b) The effect of laser fluence during CLSD on the $p2/p1$ ratio (phase transition rate) at different temperatures.

by the fact that a higher system temperature provides sufficient activation energy to promote the movement and relocation of carbon atoms. In addition, the simulations at a pressure of 11 GPa with different temperatures all show low $p2$ peaks due to the lack of energy for bond reconfiguration. Based on these observations, it can be concluded that the temperature and pressure during CLSD must exceed critical values to achieve a massive phase transition. It is also worth mentioning that figure 7(g) shows the $g(r)$-r in full range (0 Å–8 Å) to confirm the long-rang ordering crystallography structure of carbon phases even under a high temperature of 0.39 eV, implying that few or no amorphous phases formed. Future work will focus on extending the integrated model to large scales to predict the size of as-fabricated NDs under various CLSD processing parameters.

By integrating the first-principle model with MD simulation, the laser fluence threshold for ND nucleation can be estimated, as shown in figure 8(a). The fairly low $p2$ peak emerging at 11 GPa in figure 7 indicates that such a pressure condition is the approximate minimum requirement for ND formation, which can be realized using CLSD with a laser fluence of ∼90 J cm^{-2}. In contrast, using LSD without confinement requires a much higher laser fluence of ∼3000 J cm^{-2} to achieve a similar pressure. These estimations were calculated within reasonable ranges by comparing them to experimental reports [12, 19, 22, 39–42]. Especially for CLSD, most experiments were carried out near the predicted threshold, despite the use of different confining media. For the LSD experiments without confinement, the applied laser fluences were much higher than the estimated threshold, as the researchers aimed to produce pressures higher than 100 GPa. Moreover, the carbon phase transition rate (or efficiency of ND nucleation) as affected by CLSD processing parameters can be quantitatively evaluated, as depicted in figure 8(b). It can be observed that the transition rate of a graphite layer with a temperature above 0.21 eV significantly increased as the laser fluence increased. For instance, given a temperature of 0.30 eV, the phase transition rate increases from 1.4% and 5.6% to 16.2% as the laser fluence increases from 100, 570–1400 J cm^{-2}. This model can be used to predict the fraction of transformed graphite under different CLSD processing parameters, and the size distribution of as-formed NDs will be reported in our future efforts by large-scale simulations. Moreover, the understanding of laser-matter interaction from this work will provide insights for advanced materials fabrication using pulsed laser energy [43–45].

5. Conclusion

This study investigated the underlying mechanisms responsible for nanomanufacturing of NDs during CLSD. A physics-based computational model integrating first-principles model with MD simulation was developed to describe the laser-induced thermo-hydrodynamic phenomena and the resultant carbon bond reconfiguration. The effects of laser processing parameters on ND formation were analyzed. The major conclusions are summarized as follows:

(a) The results reveal that confinement during CLSD significantly influences the material responses to laser irradiation, including the temporal and spatial evolutions of temperature, pressure, electron number density, and particle velocity, due to the presence of rigid boundaries which restrict plasma expansion. Compared to LSD without confinement, the shockwave pressure propagating in the graphite increased by roughly one order of magnitude, which promotes the ND nucleation.

(b) The formation of NDs tends to occur at the graphite layers beneath the initial surface where the material remains solid. This is because the extremely high temperature near the initial graphite surface causes material vaporization/ionization, preventing the solid-state carbon phase transition. Moreover, the ND nucleation and growth is predicted to last for only a few ns, which contributes to a synthesized particle size in a few to tens of nanometers.

(c) The laser fluence thresholds for ND synthesis were predicted and compared with experimental data. It was found that a minimum laser fluence of $\sim$90 J cm^{-2} for CLSD and $\sim$3000 J cm^{-2} for LSD is required to trigger the graphite-to-diamond transition during laser processing. In addition, the transition rate increases with increasing the laser fluence or decreasing the pulse width due to the enhanced shockwave pressure.

This study elucidates the fundamental mechanisms involved in CLSD. The knowledge gained in this work provides important insights and guidance for CLSD process design, control and optimization, leading to the scalable nanomanufacturing of NDs and other HTHP synthesized nanomaterials towards extensive applications.

Acknowledgments

Funding for this research was provided by National Science Foundation (NSF) under award numbers CMMI-1826439 and CMMI-1825739. This support is greatly acknowledged.

ORCID iDs

Xing Zhang https://orcid.org/0000-0002-5332-1241
Yiliang Liao https://orcid.org/0000-0001-7122-3920

References

[1] Mochalin V N, Shenderova O, Ho D and Gogotsi Y 2012 The properties and applications of nanodiamonds *Nat. Nanotechnol.* **7** 11–23
[2] Baidakova M and Vul A 2007 New prospects and frontiers of nanodiamond clusters *J. Phys. D: Appl. Phys.* **40** 6300
[3] Hui Y Y, Cheng C L and Chang H C 2010 Nanodiamonds for optical bioimaging *J. Phys. D: Appl. Phys.* **43** 374021
[4] Motlag M, Liu X T, Nurmalasari N P D, Jin S Y, Nian Q, Park C, Jin L R, Huang L B, Liu J and Cheng G J 2020 Molecular-scale nanodiamond with high-density color centers fabricated from graphite by laser shocking *Cell Rep. Phys. Sci.* **1** 100054
[5] Ansari S A, Satar R, Jafri M A, Rasool M, Ahmad W and Zaidi S K 2016 Role of nanodiamonds in drug delivery and stem cell therapy *Iran. J. Biotechnol.* **14** 130–41
[6] Perevedentseva E, Lin Y C, Jani M and Cheng C L 2013 Biomedical applications of nanodiamonds in imaging and therapy *Nanomedicine* **8** 2041–60
[7] Basu S, Kang W P, Davidson J L, Choi B K, Bonds A B and Cliffel D E 2006 Electrochemical sensing using nanodiamond microprobe *Diamond Relat. Mater.* **15** 269–74
[8] Greentree A D 2016 Nanodiamonds in Fabry-Perot cavities: a route to scalable quantum computing *New J. Phys.* **18** 021002
[9] Batsanov S S, Osavchuk A N, Naumov S P, Gavrilkin S M, Leskov A S, Mendis B G, Beeby A and Batsanov A S 2018 Novel synthesis and properties of hydrogen-free detonation nanodiamond *Mater. Chem. Phys.* **216** 120–9
[10] Dorokhov A O, Dolmatov V Y, Malygin A A, Kozlov A S and Marchukov V A 2020 Development of the detonation nanodiamond synthesis from tetryl based ternary mixtures *Russ. J. Appl. Chem.* **93** 1083–9
[11] Brygoo S, Henry E, Loubeyre P, Eggert J, Koenig M, Loupias B, Benuzzi-Mounaix A and Le Gloahec M R 2007 Laser-shock compression of diamond and evidence of a negative-slope melting curve *Nat. Mater.* **6** 274–7
[12] Kraus D *et al* 2016 Nanosecond formation of diamond and lonsdaleite by shock compression of graphite *Nat. Commun.* **7** 10970
[13] Yocom C J, Zhang X and Liao Y L 2018 Research and development status of laser peen forming: a review *Opt. Laser Technol.* **108** 32–45
[14] Galitskiy S and Dongare A M 2021 Modeling the damage evolution and recompression behavior during laser shock loading of aluminum microstructures at the mesoscales *J. Mater. Sci.* **56** 4446–69
[15] Zhang X, Mao B, Siddaiah A, Menezes P L and Liao Y L 2020 Direct laser shock surface patterning of an AZ31B magnesium alloy: microstructure evolution and friction performance *J. Mater. Process. Technol.* **275** 116333
[16] Mao B, Liao Y L and Li B 2018 Gradient twinning microstructure generated by laser shock peening in an AZ31B magnesium alloy *Appl. Surf. Sci.* **457** 342–51
[17] Kalentics N, Boillat E, Peyre P, Gorny C, Kenel C, Leinenbach C, Jhabvala J and Logé R E 2017 3D laser shock peening–a new method for the 3D control of residual stresses in selective laser melting *Mater. Des.* **130** 350–6
[18] Klimentov S M, Garnov S V, Konov V I, Kononenko T V, Pivovarov P A, Tsarkova O G, Breitling D and Dausinger F 2007 Effect of low-threshold air breakdown on material ablation by short laser pulses *Phys. Wave Phenom.* **15** 1–11
[19] Nian Q, Wang Y F, Yang Y L, Li J, Zhang M Y, Shao J Y, Tang L and Cheng G J 2014 Direct laser writing of nanodiamond films from graphite under ambient conditions *Sci. Rep.* **4** 6612
[20] Liao Y L, Yang Y L and Cheng G J 2012 Enhanced laser shock by an active liquid confinement—hydrogen peroxide *J. Manuf. Sci. Eng.* **134** 034503
[21] Xiong Q L, Shimada T, Kitamura T and Li Z H 2020 Atomic investigation of effects of coating and confinement layer on laser shock peening *Opt. Laser Technol.* **131** 106409
[22] Ren X D, Liu R, Zheng L M, Ren Y P, Hu Z Z and He H 2015 Graphite to ultrafine nanocrystalline diamond phase transition model and growth restriction mechanism induced by nanosecond laser processing *Appl. Phys. Lett.* **107** 141907
[23] Ren X D, Yang H M, Zheng L M, Yuan S Q, Tang S X, Ren N F and Xu S D 2014 A conversion model of graphite to ultrananocrystalline diamond via laser processing at ambient temperature and normal pressure *Appl. Phys. Lett.* **105** 021908
[24] Qiu T Q and Tien C L 1992 Short-pulse laser heating on metals *Int. J. Heat Mass Transfer* **35** 719–26
[25] Jiang L and Tsai H L 2005 Improved two-temperature model and its application in ultrashort laser heating of metal films *J. Heat Transfer* **127** 1167–73
[26] Stafe M, Marcu A and Puscas N N 2014 *Pulsed Laser Ablation of Solids: Basics, Theory and Applications* (Berlin: Springer)
[27] Zhang Z Y, Nian Q, Doumanidis C C and Liao Y L 2018 First-principles modeling of laser-matter interaction and plasma dynamics in nanosecond pulsed laser shock processing *J. Appl. Phys.* **123** 054901
[28] MacFarlane J J, Golovkin I E and Woodruff P R 2006 HELIOS-CR–A 1-D radiation-magnetohydrodynamics code with inline atomic kinetics modeling *J. Quant. Spectrosc. Radiat. Transfer* **99** 381–97
[29] Christensen B H, Vestentoft K and Balling P 2007 Short-pulse ablation rates and the two-temperature model *Appl. Surf. Sci.* **253** 6347–52

[30] Peterson R R, MacFarlane J J and Moses G A 1995 *BUCKY-1–A 1-D Radiation Hydrodynamics Code for Simulating Inertial Confinement Fusion High Energy Density Plasmas* (Madison, MI: Fusion Technology Institute University of Wisconsin)

[31] Chen F F 1984 *Introduction to Plasma Physics and Controlled Fusion* (Berlin: Springer)

[32] Stuart S J, Tutein A B and Harrison J A 2000 A reactive potential for hydrocarbons with intermolecular interactions *J. Chem. Phys.* **112** 6472–86

[33] Li X W, Wang A Y and Lee K R 2018 Comparison of empirical potentials for calculating structural properties of amorphous carbon films by molecular dynamics simulation *Comput. Mater. Sci.* **151** 246–54

[34] Todd B D and Daivis P J 2017 *Nonequilibrium Molecular Dynamics: Theory, Algorithms and Applications* (Cambridge: Cambridge University Press)

[35] Stukowski A 2009 Visualization and analysis of atomistic simulation data with OVITO–the Open Visualization Tool *Modelling Simul. Mater. Sci. Eng.* **18** 015012

[36] Ren X D, Tang S X, Zheng L M, Yuan S Q, Ren N F, Yang H M, Wang Y, Zhou W F and Xu S D 2015 Direct transfer-adsorption: the new molecular dynamics transition mechanism of nano-diamond preparation by laser shock processing *J. Cryst. Growth* **421** 1–7

[37] Sano T, Takahashi K, Sakata O, Okoshi M, Inoue N, Kobayashi K F and Hirose A 2009 Femtosecond laser-driven shock synthesis of hexagonal diamond from highly oriented pyrolytic graphite *J. Phys.: Conf. Ser.* **165** 012019

[38] Maia F C B, Samad R E, Bettini J, Freitas R O, Junior N D V and Souza-Neto N M 2015 Synthesis of diamond-like phase from graphite by ultrafast laser driven dynamical compression *Sci. Rep.* **5** 11812

[39] Kraus D *et al* 2017 Formation of diamonds in laser-compressed hydrocarbons at planetary interior conditions *Nat. Astron.* **1** 606–11

[40] Amans D, Chenus A C, Ledoux G, Dujardin C, Reynaud C, Sublemontier O, Masenelli-Varlot K and Guillois O 2009 Nanodiamond synthesis by pulsed laser ablation in liquids *Diamond Relat. Mater.* **18** 177–80

[41] Wang J B, Zhang C Y, Zhong X L and Yang G W 2002 Cubic and hexagonal structures of diamond nanocrystals formed upon pulsed laser induced liquid–solid interfacial reaction *Chem. Phys. Lett.* **361** 86–90

[42] Gorrini F, Cazzanelli M, Bazzanella N, Edla R, Gemmi M, Cappello V, David J, Dorigoni C, Bifone A and Miotello A 2016 On the thermodynamic path enabling a room-temperature, laser-assisted graphite to nanodiamond transformation *Sci. Rep.* **6** 35244

[43] Zhang D S, Wu L C, Ueki M, Ito Y and Sugioka K 2020 Femtosecond laser shockwave peening ablation in liquids for hierarchical micro/nanostructuring of brittle silicon and its biological application *Int. J. Extreme Manuf.* **2** 045001

[44] Nakata Y, Hayashi E, Tsubakimoto K, Miyanaga N, Narazaki A, Shoji T and Tsuboi Y 2020 Nanodot array deposition via single shot laser interference pattern using laser-induced forward transfer *Int. J. Extreme Manuf.* **2** 025101

[45] Grigoropoulos C P 2019 Laser synthesis and functionalization of nanostructures *Int. J. Extreme Manuf.* **1** 012002